

<https://doi.org/10.1038/s44304-025-00085-4>

Assessment of freeze-thaw erosion by retrogressive thaw slump on the Qinghai-Tibet Plateau combined with geophysical methods

**Chenglong Jiao¹, Fujun Niu²✉, Peifeng He³, Jing Luo⁴ & Fan Yu⁴**

Retrogressive thaw slumps (RTSs) are significant thermokarst features in alpine permafrost environments of Arctic regions and the Tibetan Plateau (QTP), China. These formations contribute substantially to freeze-thaw erosion and organic carbon release, affecting regional ecological dynamics. Despite their importance, geophysical evidence of freeze-thaw erosion in RTS development areas remains limited due to challenging access and insufficient multi-methodological analyses. This study presents a high-resolution geophysical investigation of RTS development in the Beiluhe River Basin, QTP. Using a multi-methodological approach, we quantitatively assess freeze-thaw erosion processes by characterizing lithostratigraphy, ground ice distribution, hydrogeological properties, and deformation patterns across the RTS. Our findings reveal that freeze-thaw processes and lateral thermal erosion from the headwall create significant heterogeneity in soil hydraulic properties along the development direction, with an estimated total volume change of approximately 13,139 m³ in the studied area. These insights illuminate the complex freeze-thaw processes driving RTS development and their ecological implications across the QTP.

Retrogressive thaw slumps (RTSs) represent one of the most dynamic and visually striking manifestations of permafrost degradation in cold regions^{1,2}. These thermokarst landforms develop when the thawing of ice-rich permafrost initiates active layer detachment failure^{3,4}, creating distinctive crescent-shaped depressions characterized by an actively retreating headwall and a liquefied slump floor^{5–7}. While RTSs have been extensively documented across Arctic regions^{1,8,9} and increasingly on the Qinghai-Tibet Plateau (QTP)^{2,10–12}, the quantitative assessment of their freeze-thaw erosion processes remains limited, particularly in high-altitude permafrost environments.

The significance of RTSs extends beyond their geomorphological characteristics. They represent critical agents of landscape transformation that influence multiple environmental systems simultaneously. First, RTSs accelerate permafrost degradation through exposing previously insulated ice-rich layers to direct atmospheric conditions, creating positive feedback loops that can dramatically alter local thermal regimes^{9,13–15}. Second, they function as conduits for substantial sediment, nutrient, and carbon

mobilization, with direct implications for downstream aquatic ecosystems^{16,17}. Third, the release of previously sequestered organic carbon during RTS development may contribute to greenhouse gas emissions, potentially creating additional climate feedback mechanisms^{18–20}.

On the QTP (Fig. 1), which contains the largest high-altitude permafrost region globally, RTSs have emerged as increasingly common features, particularly in ice-rich permafrost zones^{10,11,21}. Recent authors' studies have documented approximately 2669 active RTSs across the QTP^{10,22}, indicating the widespread nature of this disturbance mechanism. These features are particularly concerning given that the QTP has experienced warming rates approximately twice the global average over recent decades^{23–25}, making it especially vulnerable to thermally-driven landscape changes.

While previous investigations have employed various approaches to characterize thermokarst landforms—ranging from field observations^{3,26,27} to geophysical techniques^{28–30} and remote sensing analyses^{31–35}—few studies have integrated multiple complementary methods to comprehensively assess freeze-thaw erosion processes in RTSs development area.

¹School of Railway Engineering, Guangzhou Railway Polytechnic, Guangzhou, 511300, China. ²Green and Intelligent Prevention Institute of Geological Disasters, School of Environment and Geographic Sciences, Shanghai Normal University, Shanghai, 200234, China. ³School of Civil Engineering and Transportation, South China University of Technology, Guangzhou, 510641, China. ⁴State Key Laboratory of Cryospheric Science and Frozen Soil Engineering, Northwest Institute of Eco-Environment and Resources, Chinese Academy of Sciences, Lanzhou, 730000, China. ✉e-mail: niuf@shnu.edu.cn

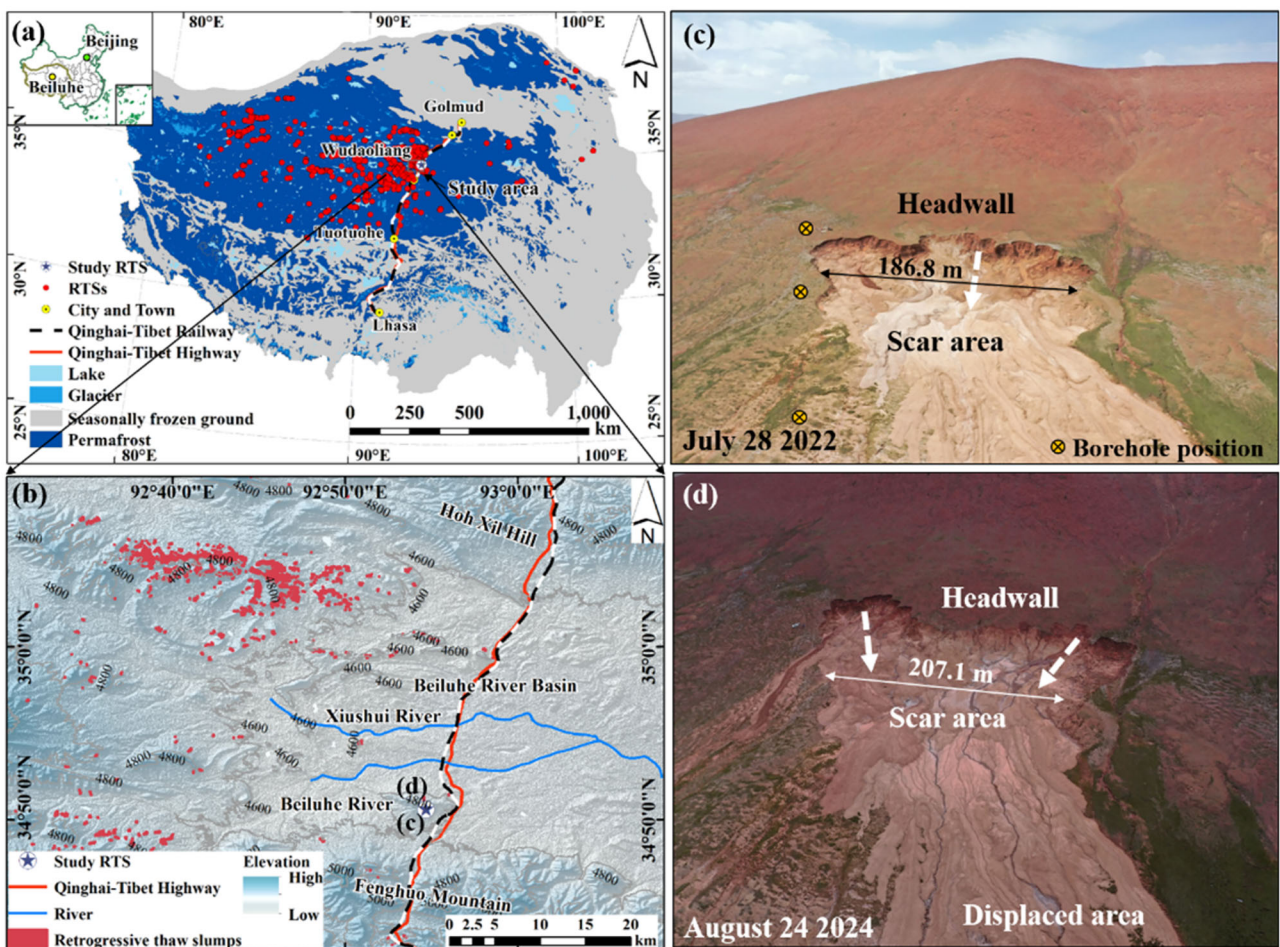


Fig. 1 | Location of the studied retrogressive thaw slump (RTS) on the Qinghai-Tibet Plateau (QTP). **a**, Spatial distribution of a permafrost and active RTSs on the QTP based on the Interpreted Active RTSs Data⁵⁷ and the QTP Science Data Center for China, National Science & Technology Infrastructure; **b**, the terrain map of the research region¹⁵ (reproduced with permission, copyright 5991170235978, 2019); **c, d**, the detail of the studied RTS developed on the north slope of the Gerlama Hill in the Beiluhe River Basin.

Geophysical methods hold particular promise as non-destructive approaches to characterize subsurface conditions^{29,36}. Electrical resistivity tomography (ERT) has effectively mapped ground ice distribution and permafrost conditions^{2,37,38}. Ground penetrating radar (GPR) has demonstrated utility in delineating active layer thickness and subsurface structures^{39–41}. Nuclear magnetic resonance (NMR) provides valuable insights into unfrozen water content and soil hydraulic properties^{42,43}. Meanwhile, high-resolution surface models derived from unmanned aerial vehicle (UAV) photogrammetry and terrestrial laser scanning (TLS) enable precise quantification of volumetric changes and headwall retreat rates^{5,44}.

The integration of these complementary techniques offers a powerful approach to characterize RTS dynamics comprehensively. However, such integrated studies remain rare, particularly in the challenging field conditions of the QTP. Additionally, while these methods have proven valuable individually, their coordinated application specifically to quantify freeze-thaw erosion processes in RTSs represents a novel methodological approach with significant potential to advance our understanding of these thermokarst landforms.

This study seeks to refine and expand existing frameworks by employing a systematic, multi-methodological, and high-resolution investigation of a representative RTS in the Beiluhe River Region (BLH) of the QTP (Fig. 1). Specifically, we aim to: (1) characterize the lithostratigraphy and ground ice distribution within and surrounding the RTS; (2) assess the hydrogeological properties across the RTS development zone; and (3) quantify the deformation and volumetric changes associated with RTS evolution. By integrating drilling data with ERT, GPR, NMR, and high-

resolution topographic measurements from UAV photogrammetry and TLS, we provide insights into the freeze-thaw erosion processes driving RTS development in this region. The findings from this study not only enhance our mechanistic understanding of RTS dynamics on the QTP but also establish a methodological framework for future evaluations of thermokarst-induced landscape changes across permafrost regions globally.

Results

Based on a combined investigation using in situ geophysical detection and TLS-UAV scanning measurements, a comprehensive assessment was conducted on the soil hydraulic properties, soil stratigraphy, and the spatial distribution of ground ice in development area of the Gu-hill RTS. The aim was to qualitatively analyze the soil freeze-thaw erosion characteristics and thermal disturbances during the development and evolution of typical RTSs, providing geophysical evidence and quantitatively estimating deformation and volumetric changes throughout the development process. This assessment reflects soil erosion due to freeze-thaw erosion. The research findings also provide a basis and validation for numerical simulation studies on the development and evolution of RTSs.

Soil hydraulic conductivity and hydrological changes in the active layer

Understanding the hydraulic properties of soil near the active layer and the permafrost table (2–3 m below the permafrost table) is essential for investigating moisture migration processes during the development and evolution of RTSs. Figure 2 presents the distribution of $\log_{10}T_2$ and the

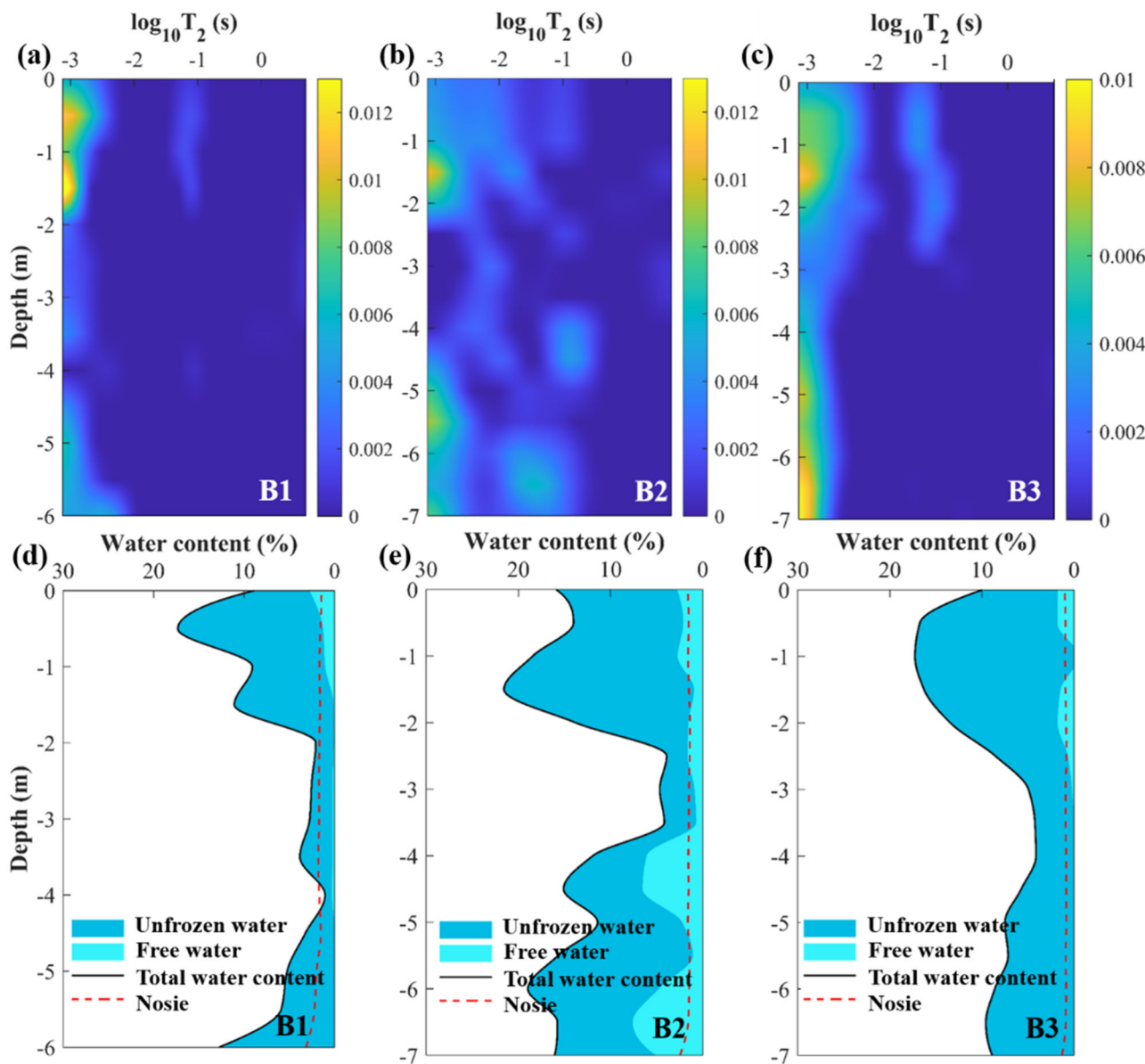


Fig. 2 | Inversion results from surface NMR sounding in the Gu-hill RTS. **a–c** Decay time and water content distribution for boreholes B1 to B3; **d–f** unfrozen water content distribution.

variation in water content within the 0–7 m depth range below the surface at three boreholes (B1–B3) located on the eastern side of the Gu-hill RTS area (aligned along the north-south direction, as shown in Fig. 1a). As shown in Fig. 2a, c, the T_2 time distribution with borehole depth, depicted by alternating light and dark patterns, indicates changes in water content. Brighter areas correspond to higher water content at those depths. In borehole B1 (Fig. 2a), within the 0–1.8 m depth range, the higher energy on the left side of the X-axis at $\log_{10} T_2 = -3$ indicates small pore water, while fluctuations in water content on the right side at $\log_{10} T_2 = -1$ represent large pore water. Below a depth of 2 m, only small pore water is observed. In borehole B2 (Fig. 2b), when $\log_{10} T_2$ ranges from -2.5 to -1, the water content is significantly higher than in the other two boreholes, indicating large pore water. This could be due to borehole B2's proximity to the landslide area, where soil freeze-thaw erosion and thermal disturbances from the Gu-hill RTS have altered the unfrozen water content distribution. Borehole B3 mainly contains small pore water, with large pore water distribution observed only within the 0–2.8 m depth range. This suggests that ground ice is more prone to melting near the headwall.

As shown in Fig. 2d–f, the water content in the active layer soil (0–2.2 m) generally increases initially and then decreases. The depths at which the highest water content occurs in the three boreholes are 0.5 m, 1.4 m, and 1.2 m below the surface, with corresponding water contents of 17.8%, 21.6%, and 18.2%, respectively. The locations of boreholes B2 and B3 correspond to the landslide area, where soil freeze-thaw erosion caused by the slump has led to the migration of fine particles in the 0–1 m depth range, resulting in significant mudflow material on the slump surface. This accelerates moisture migration downward during the thawing season, leading to relatively high water content at 1 m below the surface in these two boreholes. Additionally, the active layer soil in borehole B2 exhibits higher free water content, distributed throughout the entire borehole. This may be due to water supply from both precipitation and the melting of ground ice, as borehole B2 is closer to headwall.

Within the 2.5 m range below the permafrost table, the measured water content represents the unfrozen water content of permafrost, ranging from approximately 4.8% to 8%, due to the presence of massive ground ice or ice-rich permafrost. As the depth increases and the ice-rich permafrost transitions to ice-poor permafrost, the soil water content gradually

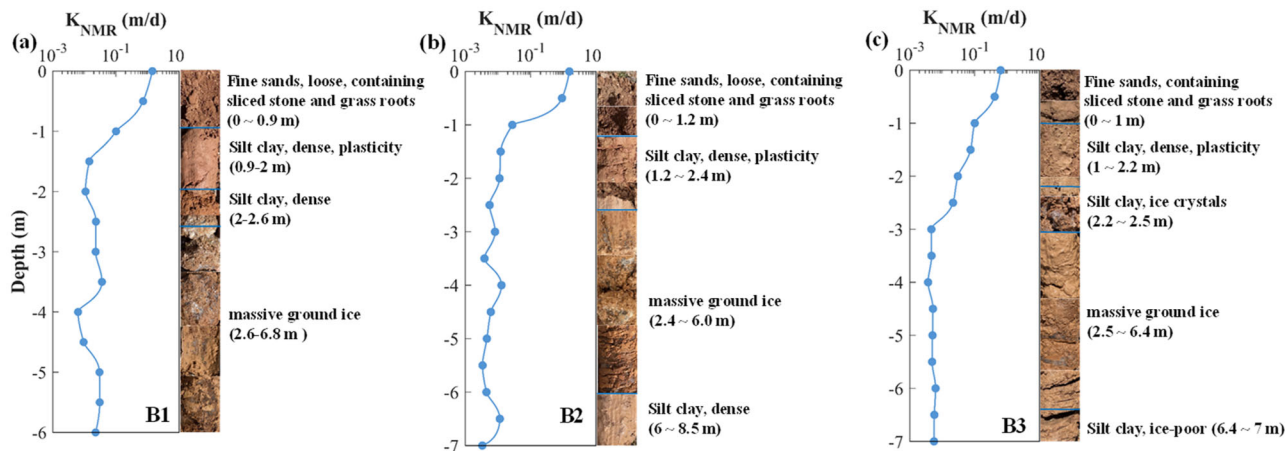


Fig. 3 | Soil permeability coefficients and stratigraphic distribution of boreholes B1 to B3 near the Gu-hill RTS. a Borehole B1; b borehole B2; c borehole B3.

increases, with unfrozen water content exceeding 10%. The unfrozen water contents in the massive ground ice and ice-rich permafrost depth ranges for the three boreholes are 3.5–5%, 5–7.2%, and 5.2–7.4%, corresponding to depths of 2.2–4.6 m, 2.6–3.8 m, and 2.9–4.1 m below the surface, respectively. Soil freeze-thaw erosion and lateral thermal erosion induced by the RTS development have prolonged the recovery time of permafrost and weakened the ice segregation process. By comparing the field-measured water content (Fig. 12c) with the NMR-inverted water content (Fig. 2), the NMR-measured water content in the active layer soil is slightly lower than the field-measured values, showing good consistency. In the permafrost layer, this water content reflects the unfrozen water content under current ground temperature conditions (approximately -1.52°C in the permafrost layer).

In the active layer soil, alpine grass roots are predominantly distributed within 0.5 m below the surface. The soil structure is relatively loose due to the presence of fine sand and organic matter, especially at the surface, where the high organic matter content results in a larger soil permeability coefficient. As illustrated in Fig. 3 all three boreholes exhibit relatively high soil permeability coefficients, ranging from approximately 0.5 to 1.04 m/d. The distribution of silty clay in the study area generally spans the 1.0 to 2.5 m depth range, except for borehole B2, where fine sand with minor inclusions of clay and gravel is primarily found within the 1.2 to 1.8 m range. Consequently, a relatively high permeability coefficient is observed, reaching a maximum of 0.1 m/d at 1.2 m depth. Below 2.5 m, the presence of thick subsurface ice or ice-rich permafrost results in a decreased permeability coefficient, ranging from approximately 0.01 to 0.001 m/d.

Ground ice distribution and ablation characteristics

Figure 4 presents the interpreted results of the geophysical survey profile G1 (see Fig. 10a), corresponding to the three boreholes on the eastern side of the Gu-hill RTS. The inversion and iterative results of the resistivity model (Fig. 4a) indicate that the active layer is approximately 2.5 m, with resistivity values ranging from about 100 to 1000 Ωm within this depth. The resistivity of the active layer exhibits some fluctuations due to variations in soil moisture content: in the area near borehole B3 (along the survey line from 125 to 175 m), resistivity values are lower, less than 200 Ωm . In the sections along the survey line from 20 to 58 m and 60 to 146 m, the resistivity values in the depth range of 2.5 to 7.5 m below the surface are relatively high, approximately 6000 to 20,000 Ωm , which can be interpreted as massive ground ice or ice-rich permafrost. Between 0 and 155 m along survey line G1, the presence of unfrozen water within the massive ground ice results in stronger radar signal amplitudes and discontinuous isophase reflections, manifesting as diffraction curves (Fig. 4b, c). The high resistivity values of the massive ground ice enhance the radar signal strength. As depth increases, resistivity gradually decreases, with values ranging from approximately 40 to 500 Ωm at depths exceeding 7.5 m. Within this depth

range, radar reflection signal amplitudes are observed to be weaker and waveforms more uniform, though occasional sharp peaks are detected between 7.5 to 9 meters. Borehole data (Fig. 12b) suggests that this interval can be interpreted as densely weathered mudstone containing minor gravel or ice crystals. Additionally, when the survey line distance surpasses 155 m, the resistivity values diminish by 2 to 3 orders of magnitude in comparison to the first 150 m of the profile, where resistivity values are approximately 600 to 1500 Ωm .

Understanding the distribution of ground ice behind the headwall of the Gu-hill RTS (south of the headwall) is crucial for analyzing the future development and freeze-thaw erosion of RSTs. Figure 5 presents the interpreted results of the ERT and GPR geophysical surveys at a location approximately 2.5 m from the edge of the Gu-hill RTS headwall, along profile G2. The resistivity model (Fig. 5a) indicates high resistivity values, approximately 4000 to 20,000 Ωm , at 0–50 m and 150–190 m along the survey line (east-west direction). In contrast, the resistivity values at 50–150 m are relatively low, ranging from 1000 to 3500 Ωm . The high resistivity values suggest the presence of massive ground ice layers, approximately 5 to 8 m thick, on the southern side of headwall. The ground ice on the eastern side of the Gu-hill RTS are thicker and contain higher ice content, with an estimated ice content of approximately 68%, based on similar findings in the Canadian permafrost region²⁸. The GPR survey interpretation results (Fig. 5b) show strong discontinuities in the isophase reflections within the 0–60 m and 155–185 m ranges, indicating the presence of massive ground ice containing unfrozen water at depths of 1.9 to 9 m. In contrast, the radar signal amplitude is relatively weak within the 60–155 m range along the survey line. This distribution pattern suggests that the survey line at 50–155 m is closer to the edge of the headwall, where ground ice has melted, potentially leaving coarse debris deposits or residual ground ice. These findings confirm that thermal disturbances and freeze-thaw erosion are more intense in this area, resulting in greater retreat distances of the headwall. The integrated geophysical survey results indicate the distribution of massive ground ice or ice-rich permafrost along the survey line as follows: at 0–50 m, the thickness ranges from approximately 2 to 10 m; from 50 to 155 m, the thickness varies between 2.5 and 6.5 m; and from 155 to 190 m, the thickness spans approximately 2.1 to 8.5 m.

Quantitatively assessment of soil erosion

To quantitatively estimate soil erosion in the Gu-hill RTS, primarily manifested as deformation and volumetric changes, this study utilized multi-temporal deformation investigation methods to construct high-resolution orthophotos, digital elevation models (DEMs), and Triangular Irregular Network (TIN) models. A comparative analysis was conducted on the changes in the outer contours and TIN grid coordinates of the Gu-hill RTS development area between 2021 and 2022.

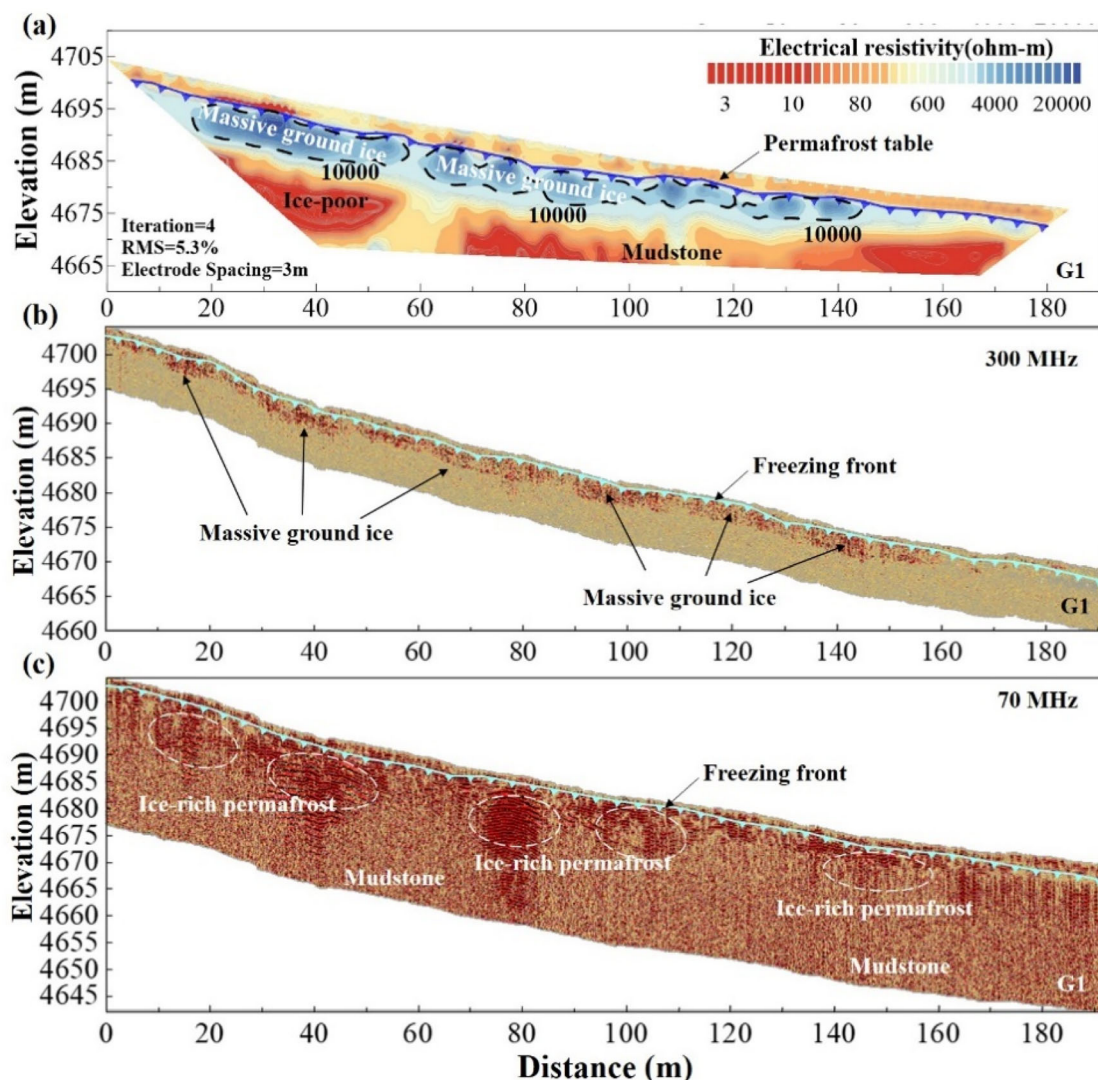


Fig. 4 | Geophysical survey interpretation profiles of the Gu-hill RTS area. a Interpretation profile from ERT; **b** interpretation profile from 300 MHz GPR; **c** interpretation profile from 70 MHz GPR.

Figure 6 illustrates the deformation and volumetric changes in the Gu-hill RTS between 2021 and 2022, including the retreat displacement of the headwall, ground deformation within the slump area and its adjacent impact zones, and volumetric changes during the evolution process (primarily manifested as soil erosion). The blue and light yellow contour lines represent the outer boundaries of the slump area in September 2021 and August 2022, respectively (Fig. 6b).

Through the overlay analysis of the scan data, vertical deformation and the retreat deformation of the headwall in the affected area of the Gu-hill RTS were calculated between the two scans (Fig. 6a). Negative values in the Fig. 6 indicate erosion and thaw settlement in the development area, representing ground deformation caused by semi-circular or free-fall motion (active layer detachment) of the thawed slump materials, followed by sliding or flowing towards the front edge. Positive values represent uplifted areas within the slump region, indicating accumulated slump material after sliding.

During the interval between the two scans, the headwall area on the southwest side of the Gu-hill RTS exhibited significant retreat and ground subsidence deformation. The overlay analysis of multi-temporal investigation indicates that the “branches” of the headwall in the southeastern and southwestern parts of the slump area experienced relatively large retreat displacements, measuring 7.8 m and 8.5 m, respectively. The maximum ground subsidence occurred at the bottom of the headwall on the southwest

side, measuring approximately 3.5 m. The higher deformation at the top of the headwall reflects active layer detachment failure.

To more intuitively reflect the volumetric changes in the Gu-hill RTS development area, a comparison of the high-density point cloud data from the TLS scans over time was conducted. The occurrence of active layer detachment at the headwall resulted in the expansion of development area. As the thawed materials slid along the sliding surface of the headwall, most of it eventually settled in the “scar” area of the Gu-hill RTS, while the remaining material continued to flow. A comparative analysis of the two survey results indicates that the total volumetric change in the development area between September 2021 and August 2022 was approximately 13,139 m³. Of this, approximately 11,801 m³ of slump material remained in the “scar” area of the Gu-hill RTS.

Impact of climate change on RTS evolution

The formation and progressive of RTSs are closely linked to the ongoing warming and humidification trends observed during the thawing season. Extreme high temperatures and intense precipitation events during this period accelerate the movement of the thawing front from the surface toward the permafrost table. This thermal disturbance affects the soil layers near the permafrost table, causing the basal soil layer of the active layer to melt. Consequently, infiltrating groundwater accumulates at the interface of the ice-rich permafrost layer, generating

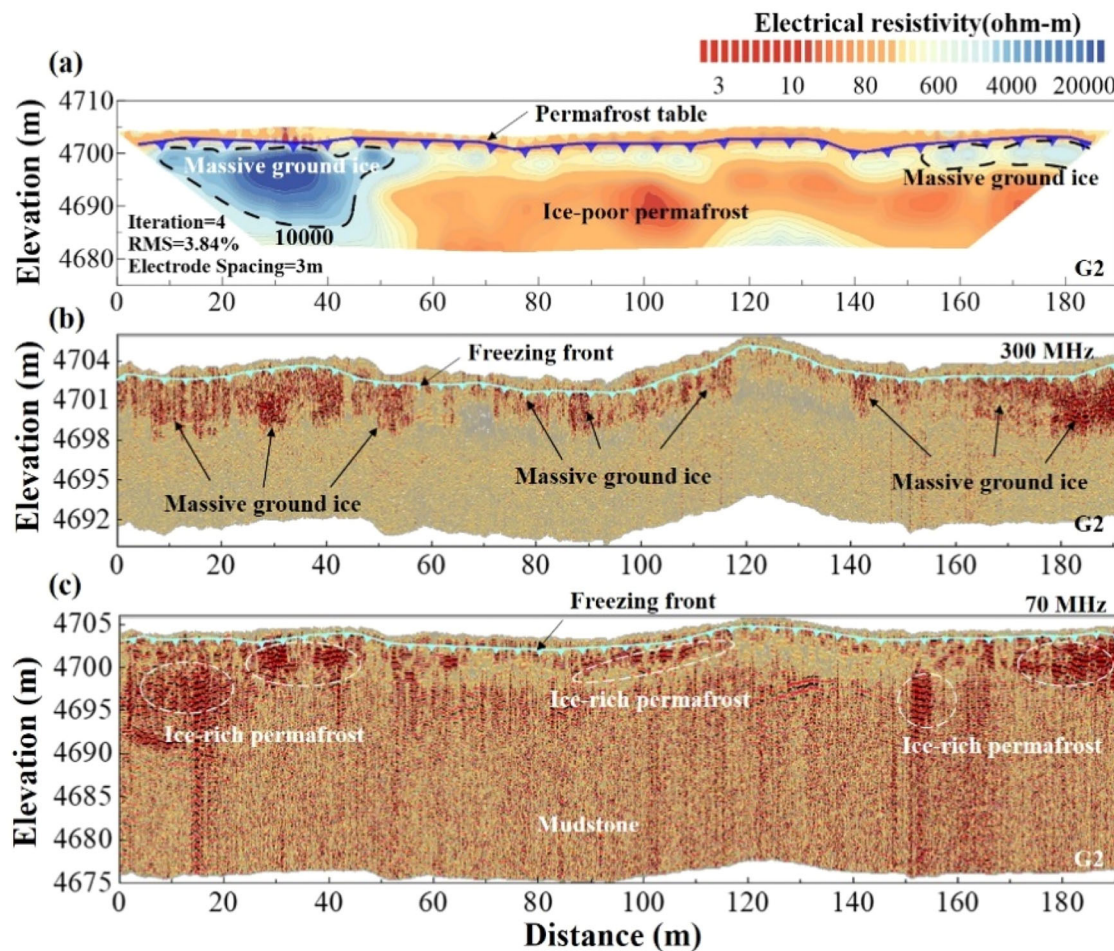


Fig. 5 | Geophysical survey interpretation profiles of the southern side on headwall of the Gu-hill RTS. a Interpretation profile from ERT; **b** interpretation profile from 300 MHz GPR; **c** interpretation profile from 70 MHz GPR.

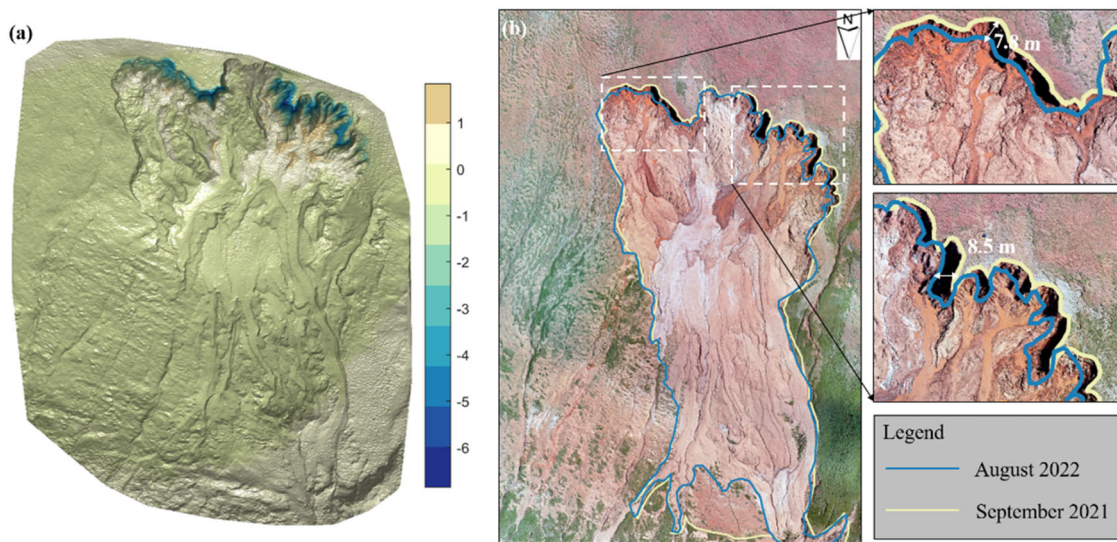


Fig. 6 | Spatiotemporal monitoring of the Gu-hill RTS using terrestrial laser scanning (TLS) and unmanned aerial vehicle (UAV). a Surface deformation; **b** headwall retrogression.

elevated pore water pressure. This pressure reduction at the interface facilitates active layer detachment. Furthermore, recurrent high temperatures and precipitation events during successive thawing seasons exacerbate the melting of exposed ground ice at the RTS headwall,

promoting the continuous development and expansion of the slump. To quantify the retreat of the Gu-hill RTS, high-resolution point cloud data collected through the TLS-UAV method were utilized to delineate the slump boundaries from 2021 to 2024 (Fig. 7). During the 2023 field

Fig. 7 | Sequence of delineated Gu-hill RTS boundary from multi-UAV data showing the RTS expansion during the observation periods. The base image is a UAV-based orthophoto of the Gu-hill RTS and the surrounding area on August, 2024.

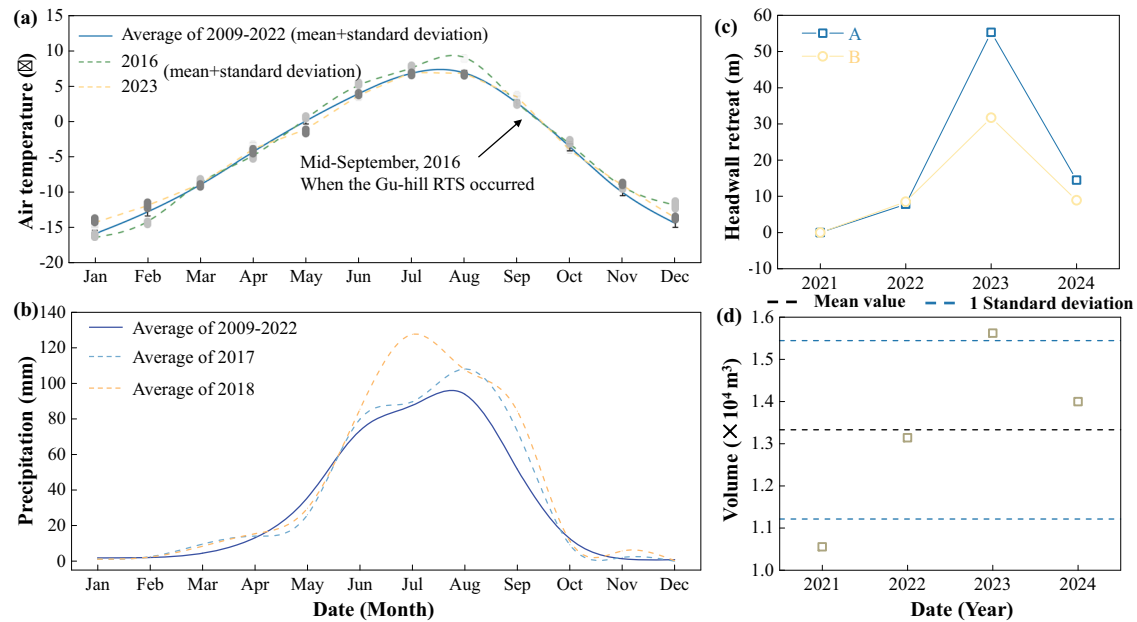
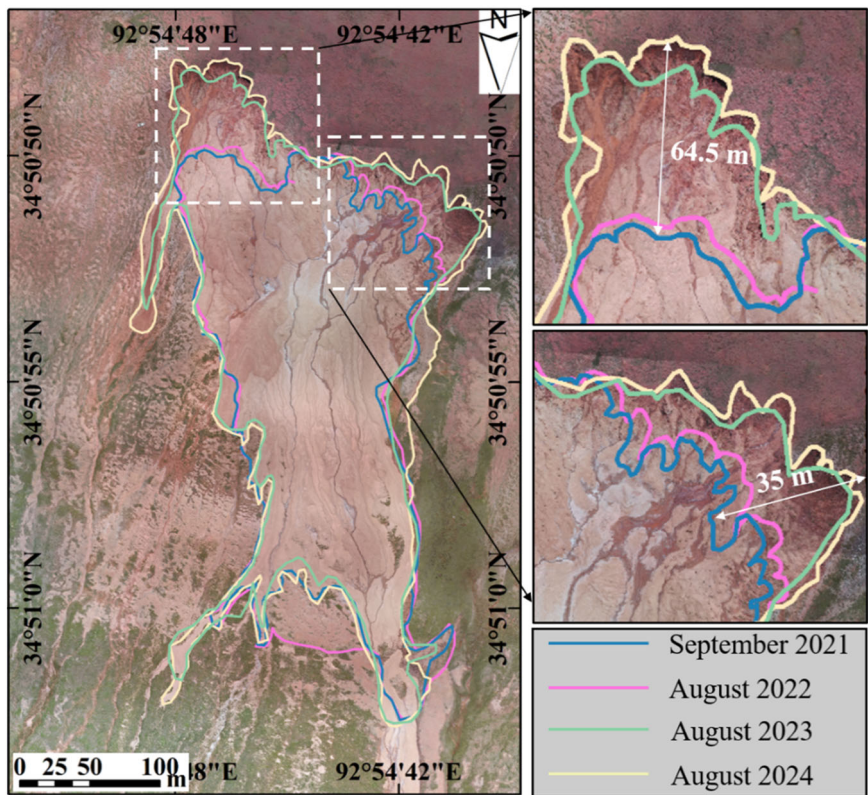


Fig. 8 | Monthly averages of temperature, precipitation, headwall retreat, and volumetric change of Gu-hill RTS in the study area. a Monthly average temperature (from 2009 to 2023); **b** monthly precipitation (from 2009 to 2023); **c** time series headwall retreats and **d** volumetric changes of two sites (A, B) from Fig. 7. (In

a, the short solid lines represent the standard deviation of the monthly average temperature from 2009 to 2022, while the gray shading indicates the standard deviation for the 2016 and 2023 average values.).

season, an unanticipated and significant mass-wasting event was observed on the eastern flank of the posterior wall of the Gu-hill RTS. The measured retrogressive displacement in 2023 was approximately 60 m eastward from the headwall, resulting in substantial sediment mobilization. A similar displacement of around 30 m was recorded on the western side of the headwall. This pronounced retreat, coupled with mass-wasting events, highlights the strong interplay between ground

ice ablation and climate variations, underscoring the critical role of climate change in driving the evolution of RTSs.

Figure 8a, b illustrates the changes in monthly average temperature and precipitation in the study area between 2009 and 2023. A comparison of the 2016 data with the 15-year average reveals that the temperatures in 2016 were notably higher than those observed from 2009 to 2022. Specifically, from June to September 2016, temperatures surpassed the 14-year average

by 0.6 to 1 °C. This period coincided with a significant detachment and instability of the active layer. Following this event, elevated precipitation levels persisted for two consecutive years (2017 and 2018) (Fig. 8b), further enhancing the freeze-thaw erosion process. From 2009 to 2023, the climate data demonstrate a clear warming trend, with particularly pronounced temperature increases during the summer months (Fig. 8). These climate shifts, in combination with heightened precipitation, have likely accelerated the degradation of ice-rich permafrost, fostering more frequent and severe retrogressive thaw slump (RTS) activity. The large-scale retreat observed in 2023 aligns with these climate anomalies, particularly the higher-than-average temperatures and increased precipitation levels. Notably, Fig. 8c, d provides a quantitative assessment of this phenomenon, showing the retreat of the RTS headwall and volumetric changes from 2021 to 2024, with the most significant displacements and mass-wasting events occurring during the 2023 field season. The increased retreat and volume changes in 2023 can be directly attributed to the elevated ground temperatures and the heightened hydrological disturbance observed during the year, reinforcing the hypothesis that RTS evolution is increasingly driven by the interaction of ground ice ablation and climate-induced thermal and hydrological disturbances.

The combination of extreme high temperatures during the thawing season and sudden increases in rainfall further accelerated the development and evolution of RTSs. Anomalously high temperatures have contributed to the deepening of the active layer and a reduction in ground ice content at the top of the permafrost, signaling ongoing permafrost degradation. Concurrently, infiltration of rainwater has facilitated the transfer of heat to the upper permafrost layer, promoting the melting of ground ice within the ice-rich transient layer. This process induces a buildup of pore water pressure at the interface between the active layer and the permafrost, leading to active layer detachment. The rise in temperatures, coupled with increased rainfall events during the thawing season, has thus accelerated both the melting of ground ice and the retreat of RTS headwalls, resulting in the expansion of affected areas and consequently intensifying the occurrence of freeze-thaw erosion processes^{2,27}.

Freeze-thaw erosion processes in RTS development

This study focuses on the Gu-hill RTS located in the BLH River Basin of the QTP, which is primarily induced by active layer detachment. The Gu-hill RTS manifests on gentle slopes with gradients ranging from 5° to 9°, representative of numerous RTSs on the Qinghai-Tibet Plateau (QTP) in terms of dimensional parameters and morphological characteristics, typically comprising high-density, fine-grained soils and sediments. These characteristics enhance groundwater retention within the soil, increasing the water content in the upper permafrost layer and promoting ice segregation. Consequently, this results in the formation of massive ground ice layers in the region.

Through a multi-method integrated investigation, this study demonstrates that during the thawing season, groundwater continuously accumulates in the active layer of the Gu-hill RTS development zone. This accumulation leads to increased pore water pressure within the active layer, which reduces friction between the active layer and the underlying permafrost table. As a result, the shear strength at the interface between the active layer and permafrost diminishes, facilitating the detachment of the active layer in this gentle slope region. While the Gu-hill RTS area is larger than the average RTS development zone across the plateau, its key characteristics—such as the steep frozen rear walls and the accumulation of mudflow material—are representative of the freeze-thaw erosion processes observed in RTSs throughout the plateau. The observed differences in RTS development areas can largely be attributed to variations in ground ice conditions; however, the underlying mechanisms driving the development and evolution of these systems remain consistent across the region. The primary cause of RTS formation in this area is the inadequate drainage or percolation of meltwater from the ground ice. This leads to a reduction in shear strength at the interface between the active layer and the ground ice, eventually triggering the detachment and instability of the active layer soil.

Following the detachment of the active layer, the exposure and further melting of ground ice at the RTS headwall facilitate the downslope movement of melted slump material and meltwater sediments.

In general, the QTP is highly susceptible to RTS-induced freeze-thaw erosion, a process characterized by the melting of ground ice, mass wasting, and significant soil erosion. The developmental characteristics and conditions of RTSs in this region are influenced by an intricate interplay of environmental and climate factors, including ground ice content, active layer dynamics, and seasonal thawing patterns. The freeze-thaw erosion process begins with the melting of ground ice, which produces a slurry of water and sediment highly prone to mass wasting. The meltwater, generated by the thawing ground ice, exacerbates the erosion process by lubricating the soil and promoting its downslope movement. Concurrently, thaw-induced mass wasting involves the downslope movement of large quantities of thawed, saturated soil and debris, driven by gravitational forces. This results in significant soil displacement and landscape alteration. The accumulation of melted slump material and meltwater sediments at the slump's base further contributes to instability, perpetuating the evolution of the RTS. The detachment and subsequent movement of the active layer result in the displacement of substantial volumes of soil, leading to the loss of terrestrial habitat and alterations in local hydrological systems. Additionally, this erosion process can increase sediment loads in nearby water bodies, thereby impacting water quality and aquatic ecosystems.

Discussion

Through extensive field investigations, borehole drilling, and geophysical surveys conducted by our research team in recent years in the BLH River Basin, we have observed that most RTSs in the permafrost regions of the QTP are predominantly triggered by active layer detachment. These freeze-thaw erosion processes have a profound impact on the ecological environment of the QTP, with significant soil erosion as a primary manifestation. Moreover, the development and evolution of RTSs are influenced not only by topographical features but also by the permafrost conditions in the region, including the hydrological dynamics of the active layer and the spatial distribution of ground ice. The ongoing warming and increasing humidity across the plateau have further exacerbated the formation and expansion of RTSs.

Building upon the established correlations between climate variables and RTS volumetric changes presented in *Impact of Climate Change on RTS Evolution*, we can now elaborate on the specific permafrost response mechanisms that mediate these climate-erosion relationships. Over the past decade, the QTP has experienced five major responses in permafrost dynamics that directly contribute to freeze-thaw erosion processes: permafrost degradation, active layer deepening, ground ice melting, increased pore water pressure, and reduced soil shear strength²⁷. These mechanisms explain how the climate warming trends and precipitation patterns quantified earlier translate into the observed accelerated erosion rates across the plateau. Collectively, these processes have triggered a significant increase in RTS activity across the plateau. Notably, this surge has not been uniform across years; rather, it has been concentrated during periods of intensified climate warming and increased humidity.

Through our multi-methodological investigation of the Gu-hill RTS, we have quantified how these permafrost responses manifest in measurable erosion impacts. Our geophysical analysis has delineated key stratigraphic features, soil hydraulic properties, unfrozen water content, and ground ice distribution that control freeze-thaw erosion susceptibility in a typical RTS development area. Active layer detachment emerges as the primary mechanism initiating freeze-thaw erosion, with ground ice at the RTS headwall playing a critical role. As ground ice at the RTS headwall continues to thaw, the soil at the headwall undergoes further destabilization, leading to free-fall or semi-circular motion along the slump surface. This movement drives the downslope sliding and flow of collapsed ground ice and meltwater sediments.

The geophysical approach demonstrated in this study provides quantitative evidence for assessing freeze-thaw erosion processes associated with RTS development. By connecting the five permafrost response mechanisms to specific erosional outcomes, our findings contribute essential data for understanding thermokarst-induced soil erosion and enhance our capacity to evaluate climate-driven erosion hazards in permafrost regions across the QTP and similar environments globally.

Notwithstanding the significant contributions to understanding RTS-related freeze-thaw erosion processes, this investigation is subject to several methodological constraints. Our site selection was based on statistical analysis of 2669 active RTS across the QTP, from which we selected a single representative RTS for comprehensive geophysical investigation. Although this approach yielded significant quantitative data, the influence of localized developmental factors limits direct extrapolation of our findings to the entire plateau. The quantification of RTS volume changes, critical for assessing soil erosion under freeze-thaw processes, was conducted using TLS-UAV surveys during the thawing seasons (August or September) from 2021 to 2024. However, our study lacks detailed analysis of complete life-cycle changes within individual thawing seasons, which would provide more granular insights into freeze-thaw erosion dynamics.

Despite these constraints, our methodology offers a novel approach for quantitatively assessing freeze-thaw erosion processes associated with RTS on the QTP and serves as a valuable reference for similar research in other permafrost regions. Nevertheless, the current approach is impractical for quantifying freeze-thaw erosion across the entire QTP, as regional-scale assessment requires more efficient methodologies. To address these limitations, future research will focus on integrating comprehensive geophysical data with remote sensing method to develop more practical estimation models for freeze-thaw erosion in permafrost regions. Through extensive remote sensing data analysis, researchers can more efficiently and accurately estimate the freeze-thaw erosion effects of RTS across larger geographical areas. This methodological integration would significantly advance our scientific understanding of climate-permafrost interactions on the QTP and analogous high-altitude ecosystems where RTS proliferation constitutes a critical indicator of cryospheric response to warming trends.

Overall, this study presented a comprehensive geophysical investigation of freeze-thaw erosion processes associated with RTS development on the QTP. Through the integration of multiple complementary methodologies—including drilling, NMR, GPR, ERT, UAV photogrammetry, and TLS—we characterized the internal structure, hydrological properties, and volumetric changes of a representative RTS in the BLH River Basin. This multi-methodological approach enabled us to quantitatively assess freeze-thaw erosion processes and provided valuable geophysical evidence for understanding the environmental implications of RTS development. Our findings elucidate several key aspects of RTS dynamics in this region.

The integration of drilling, NMR, GPR, and ERT measurements revealed the complex internal structure of the RTS, including the distribution of ground ice, active layer properties, and lithological characteristics. This integrated approach proved effective for characterizing the subsurface conditions that control RTS development. Furthermore, soil hydraulic properties exhibit significant spatial heterogeneity across the RTS, with permeability coefficients ranging from $0.5\text{--}1.04\text{ m d}^{-1}$ in the near-surface (0–0.5 m depth), decreasing to approximately 0.1 m d^{-1} at intermediate depths (0.5–2.5 m), and further reducing to $0.01\text{--}0.001\text{ m d}^{-1}$ below 2.5 m where ice-rich permafrost predominates. These patterns indicate how freeze-thaw processes and lateral thermal erosion create distinct hydrological zones that influence material transport and RTS evolution.

NMR-Dart logging demonstrated that unfrozen water content within active layer soils initially increases with depth before decreasing at the permafrost table. The presence of organic matter in shallow soils appears to promote water movement in the upper active layer, facilitating the transport of thawed material. The heterogeneity in soil hydraulic properties along the RTS development direction may extend permafrost recovery time and weaken ice segregation processes. Additionally, quantitative analysis of TLS-UAV survey data between 2021 and 2022 documented maximum headwall

retreat rates of 7.8 m and 8.5 m in the southeastern and southwestern portions of the RTS, respectively. The total volumetric change during this period was approximately $13,139\text{ m}^3$, with about $11,801\text{ m}^3$ of slumped material remaining within the RTS development area.

These data and analyses advance our understanding of RTS-induced freeze-thaw erosion on the QTP by providing detailed geophysical evidence and quantitative measurements. The methodological approach developed here offers a valuable framework for future investigations of thermokarst landforms in permafrost regions. While our findings are based on a single representative RTS, they provide important insights into the mechanisms driving RTS development and associated environmental changes that can inform broader assessments of permafrost degradation impacts across the QTP and similar high-altitude permafrost regions globally.

Methods

Spatial distribution characteristics of RTSs in the QTP

The QTP represents a prominent region where ice-rich permafrost is notably prevalent within the boundaries of China (Fig. 1a)¹⁵. Regarding elevation, the QTP characterized by an average elevation exceeding 4000 m, extends geographically from the Himalayas in the southern reaches to the Kunlun-Qilian Mountains in the north (longitude $73^{\circ}18'52''\text{E}$ to $104^{\circ}46'59''\text{E}$) and spans from the Pamirs in the western sector to the Hengduan Mountains in the east (latitude $26^{\circ}00'12''\text{N}$ to $39^{\circ}46'50''\text{N}$)^{46,47}. Geomorphologically, the terrestrial landscapes within the hinterland of the QTP predominantly consist of alpine meadows and alpine deserts⁴⁸. Regarding climate considerations, over the past 50 years, the rate of temperature increase on the plateau has been approximately 0.3 to 0.4 °C/10a, resulting in a total warming of approximately 1.8 to 2.0 °C^{24,49}. Additionally, the total precipitation on the plateau has increased by approximately 20 to 120 mm, indicating an overall trend towards warmer and wetter conditions^{25,50}.

Due to its unique geological and climate features, combined with its high-altitude setting, the QTP harbors a permafrost area estimated at approximately 1.06 million km², representing over half of the global high-altitude permafrost extent^{51–53}. Permafrost on the QTP is characterized by significant ice content, a feature corroborated by field monitoring indicating that ground ice levels are primarily influenced by soil moisture availability, slope orientation, and fine-particle composition⁵⁴. Analysis of data from 164 boreholes reveals a geographical gradient across the QTP⁵⁵, with ground ice content increasing from east to west and from south to north. The areas of high ice-rich permafrost are notably situated in the Hoh Xil and Western Kunlun regions. In addition, the permafrost in the QTP, the active layer thickness typically ranges from 1 to 4 m, with an average thickness of approximately 2.2 m⁵⁶. Field monitoring data indicate that along the Qinghai-Tibet engineering corridor, the rate of increase in active layer thickness is approximately 2.2 cm/a²⁴. As ground temperatures continue to rise, resulting in deepening active layers, permafrost degradation intensifies, contributing to the widespread development of thermokarst occurrences in ice-rich permafrost areas of the QTP¹¹. However, frequent RTSs represent the predominant thermokarst processes influencing inclined landscapes in this region^{11,57}.

Through several field surveys and the manual interpretation of high-resolution remote sensing data obtained from the Gaofen-1 and Gaofen-2 satellites, Fig. 1 depicts the discovery of 2669 active RTSs in the permafrost regions of the QTP as of the year 2021⁵⁷. Based on statistical analysis, these RTSs areas exhibit varying developmental sizes ranging from 0.02 to 20 ha, with an average area of approximately 1.44 ha. The average perimeter of RTSs is around 600 m, ranging from 57 to 4850 m. As illustrated in Fig. 9a, RTSs of smaller developmental extent (area <1 ha) exhibit the broadest distribution and greatest abundance across the entire plateau, notably surpassing those with areas greater than 1 ha. Among these, the most densely populated region is observed in the BLH River Basin (Fig. 1b), where over 780 active RTSs have been identified¹¹. Correspondingly, approximately 87% of RTSs across the plateau have a perimeter of less than 1 km (Fig. 9b). Similarly, these smaller-scale features (perimeter <1 km) are concentrated prominently in the BLH River Basin. In addition, based on statistical data

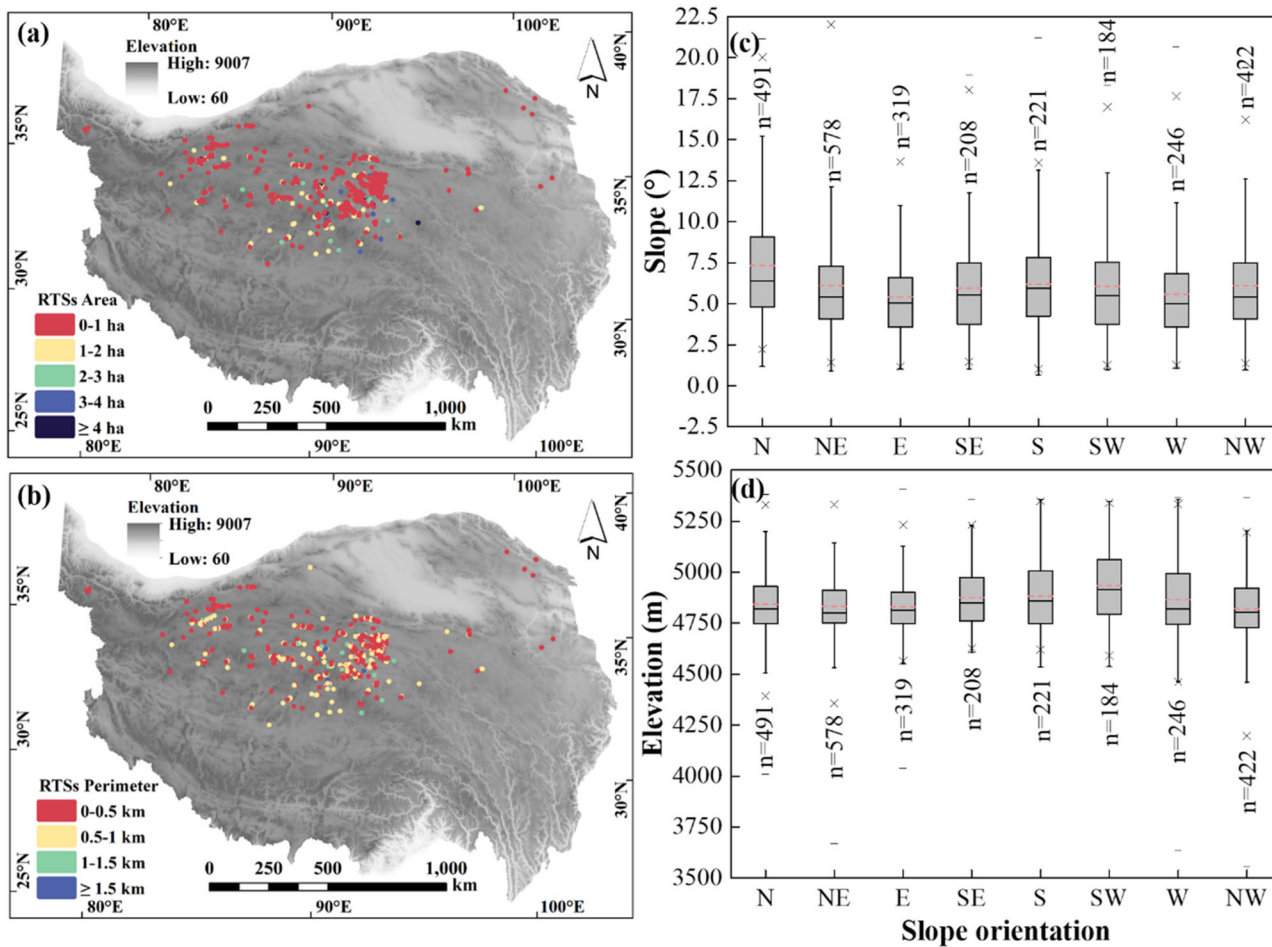


Fig. 9 | Spatial distribution characteristics of active retrogressive thaw slumps on the QTP. a Area distribution of all active RTSs; **b** perimeter distribution of all active RTSs; **c** slope distribution in regions of RTS development across different slope aspects; **d** elevation distribution in regions of RTS development across different slope aspects.

compiled up to 2021, the cumulative area affected by active RTSs on the QTP constitutes 0.00363% of the total permafrost area. This finding aligns closely with conclusions reported by Lewkowicz et al. in Arctic regions⁵⁸.

Particularly, the spatial distribution of RTSs is strongly influenced by topographical factors such as elevation, slope, and aspect. Based on statistical analyses of RTSs aspect distribution (Fig. 9c, d), although RTSs occur across all aspects of the plateau, these predominantly develop on north-facing slopes with lower solar radiation (primarily concentrated on north, $n = 491$; northeast, $n = 578$; northwest, $n = 422$). However, another significant spatial characteristic of RTSs indicate that regardless of aspect, these RTSs are primarily located between 4600 m to 5100 m elevation (Fig. 9d) and on gentle slopes ranging from 3° to 8° (Fig. 9c). These topographical parameters constitute critical scientific criteria for identifying representative RTS formations across the QTP. Therefore, considering these spatial patterns of these RTSs across the entire QTP, this study selected the BLH River Basin as the study area due to its comparatively dense distribution of RTS features that exemplify the typical morphological and dimensional characteristics observed plateau-wide.

Study area description and representativeness of Gu-hill RTS

This study examines a representative RTS formation (Fig. 1), situated in the northern Beiluhe River Basin on the QTP (34°52'55"N, 92°56'17"E) near the north-facing slopes of Gerlama Mountain (34°50'49"N, 92°54'12"E). Due to its prominence in the surrounding flat terrain, this mountain is colloquially known as “Gu Hill”. This RTS, located at the base of the northern slope of Gerlama Mountain and referred to as the Gu-hill RTS, was selected based on rigorous scientific criteria derived from our comprehensive statistical

analysis of all 2669 active RTSs across the QTP^{5,41}. The Gu-hill RTS exemplifies the predominant characteristics observed in RTSs across the plateau in several critical aspects:

Topographical setting. Located on a north-facing slope with a gradient of 5° to 9°, the Gu-hill RTS falls within the most common slope range (3° to 8°) and aspect (north-facing) where RTSs develop across the QTP as demonstrated in our statistical analysis (Fig. 9c, d).

Elevation. Situated at approximately 4750 m above sea level, the Gu-hill RTS lies within the elevation band (4600–5100 m) where the majority of RTSs across the QTP are found.

Morphological features. The Gu-hill RTS exhibits the classic crescent-shaped morphology with a steep headwall and liquefied slump floor characteristic of active RTSs across the plateau.

Development timeline

Analysis of historical remote sensing data indicates that the Gu-hill RTS occurred prior to 2016, providing sufficient temporal context to study its developmental trajectory.

While the Gu-hill RTS, with an area of approximately 3.2 ha, is larger than the average RTS on the QTP (1.44 ha), its larger dimensions enable more comprehensive geophysical investigations while still maintaining the essential morphological and developmental characteristics representative of RTSs across the plateau. Its increased size provides an advantageous setting for deploying multiple geophysical methods simultaneously, allowing for

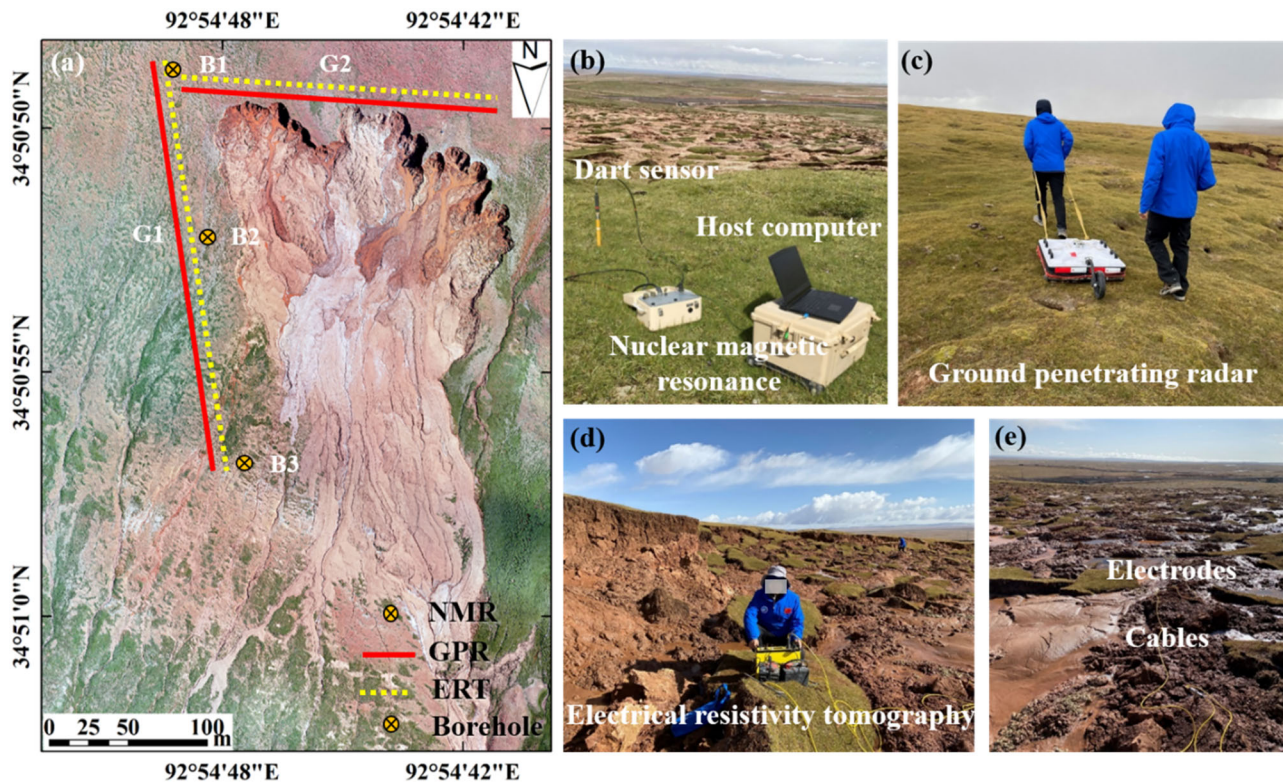


Fig. 10 | Topography, geomorphology, and layout of the field geophysical survey lines in the BLH River Basin. **a** Layout of geophysical survey lines and boreholes. B1–B3 are Nuclear Magnetic Resonance (NMR) survey boreholes and the base

map is a UAV-based orthophoto of the Gu-hill RTS and the surrounding area; **b** NMR Dart sensor; **c** ground penetrating radar; **d, e** electrical resistivity tomography.

more detailed characterization of freeze-thaw erosion processes that are fundamentally similar to those occurring in smaller RTSs.

The study area lies within a continuous permafrost zone (Fig. 1), characterized by sparse alpine meadows and deposits of fine sand and gravel. The geological strata range from surface to bedrock, comprising primarily gravel, silty clay, sandstone, and weathered mud stone⁵⁹. The overall thickness of the active layer in the region ranges from 1.5 m to 3 m, while the underlying thickness of perennially frozen ground varies from 2 m to 3 m, with a subsurface ice content of approximately 39.4%⁵⁴. Recent field surveys, analysis of historical meteorological and remote sensing data reveal the development of numerous thermokarst landforms capable of inducing significant geomorphic changes, such as RTSs, thaw subsidence, and thermokarst lakes. The region experiences an average annual temperature of about -3.28°C and an average annual precipitation of 366 mm (1990 to 2021), with the majority of precipitation occurring between May and August. The average annual evaporation is 1316.9 mm¹⁵.

To investigate freeze-thaw erosion processes through the spatial distribution of thick ground ice, high ice-content permafrost, and the permafrost table in areas affected by the selected RTS, this study employed the Advanced Geosciences Inc. AGI Supersting R8 resistivity testing system, supplemented by a dual-frequency GPR operating at 70 MHz and 300 MHz. Two measurement lines, designated as G1 and G2, were established within the RTS development region. Measurement line G1 was oriented in a north-south direction, while measurement line G2 was approximately perpendicular to it, oriented in an east-west direction (Fig. 10). GPR and ERT were utilized to conduct scanning along each geophysical measurement line (Fig. 10b–e).

To facilitate a more comprehensive interpretation of freeze-thaw erosion processes through geophysical detection data, three boreholes, named B1–B3, were drilled along the north-south measurement line, with each borehole reaching a depth of 10–15 m. Utilizing Nuclear Magnetic Resonance (NMR) technology based on borehole exploration, in situ measurements of soil moisture content and hydraulic parameters such as

soil permeability were conducted using a Dart soil moisture system sensor (Vista Clara, Inc., USA). These measurements provide critical insights into how freeze-thaw cycles alter soil hydrogeological properties and contribute to erosion processes.

Core sampling and core analysis

Toward time-series high-resolution deformation graphic information around the studied RTS, TLS and UAV photogrammetry were applied to monitor the thermokarst landforms from September 2021 through September 2022. Based on TLS-UAV investigation^{54,46}, the current survey (as of 2022) indicates that the length of the Gu-hill RTS (Fig. 11), from the headscarp to the displaced area (excluding the northwest mudflow), ranges between approximately 305 m and 324.5 m, with a maximum width of about 183 m occurring near the base of the headscarp. The total disturbed area of the slump is 46,821.3 m², with an estimated total material displacement of 81,621 m³. The headscarp, a steep frozen back scarp, of the Gu-hill RTS (Fig. 11b) is situated at an elevation of approximately 4705 m. This RTS development area extends in a north-south direction with an overall slope gradient of about 8.5° in the affected area. The Gu-hill RTS was chosen for study due to its significant scale (the area is 4.7 ha and perimeter is 1.4 km) and relatively recent formation (about 2016). And Fig. 1 illustrates the precise geographical location and aerial view of the Gu-hill RTS.

The surface of the area affected by the landslide is primarily covered by alpine meadows, with a coverage rate of approximately 6 to 19%. Based on borehole exploration and logging information 2.2 meters east of the slump scarp, the soil stratification beneath the slump scarp is depicted in Fig. 12. The layers are as follows (Fig. 12b): from 0 to 0.9 meters, there is loose reddish-brown fine sand with scattered flaky gravel, with the initial water table at 0.9 m, from 0.9 to 2.6 meters, there is relatively dense reddish-brown clay, which is plastic and contains fine sand and gravel, with the initial appearance of ice crystals at 2.1 to 2.3 m, from 2.6 to 6.8 m, there is massive ground ice, with an ice content of approximately 62 to 86%, from 6.8 to 7.6 m, there is reddish-brown clay with a 2 cm thick ice layer, initially

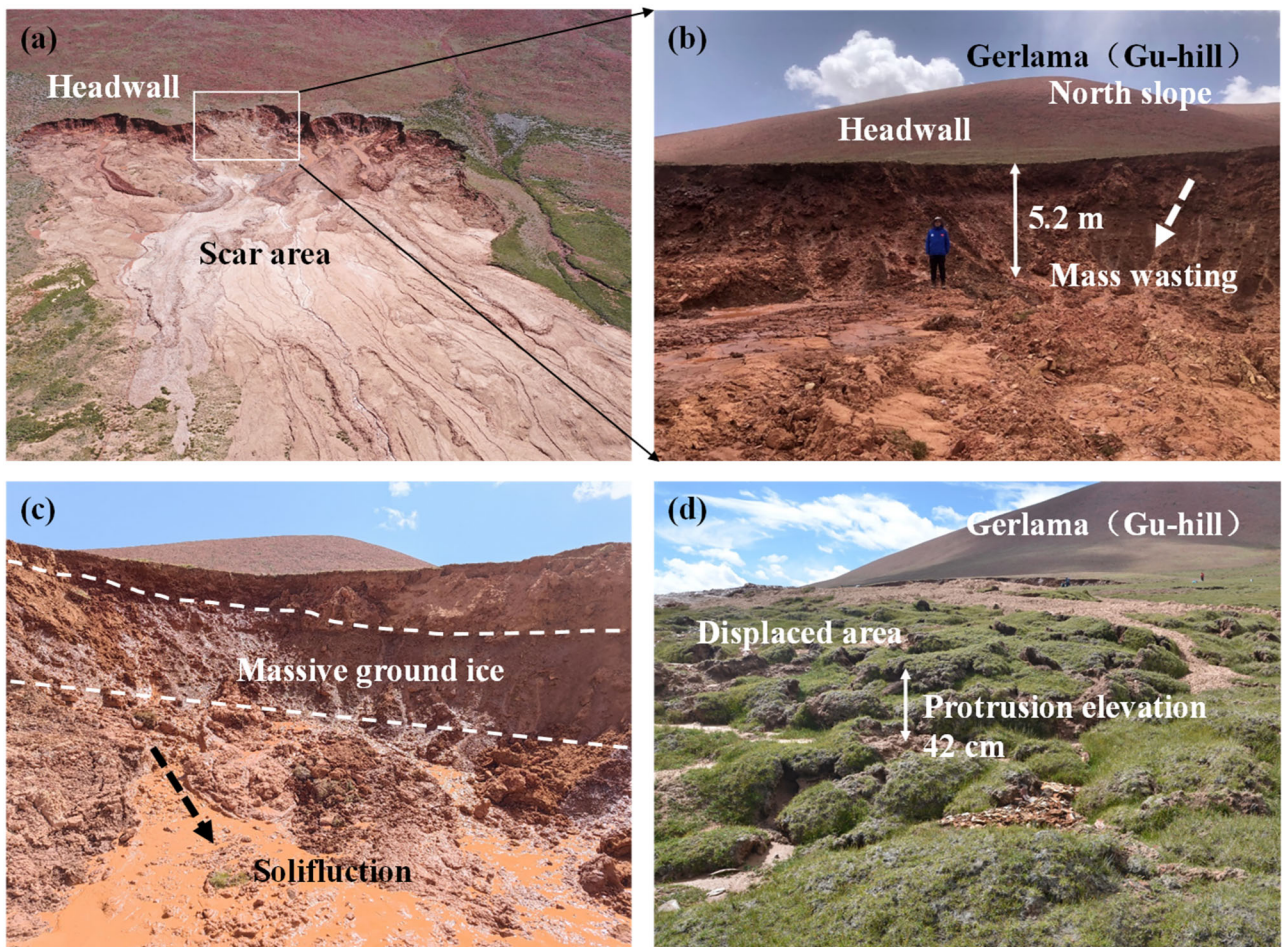


Fig. 11 | Developmental characteristics of the Gu-hill retrogressive thaw slump. **a** Aerial image of the Gu-hill RTS; **b** headwall of the slump and detached active layer material; **c** massive ground ice and mudflow material on sliding surface; **d** compression ridges developed at the toe zone of the Gu-hill RTS.

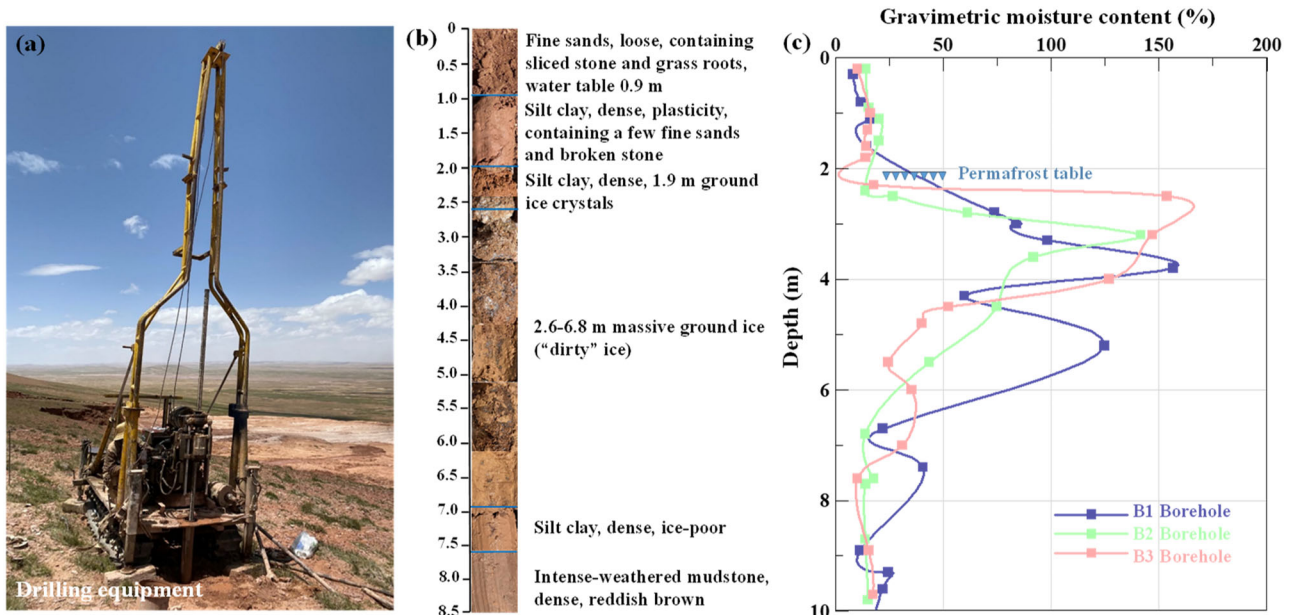


Fig. 12 | Geological borehole information of the Gu-hill RTS. **a** Photograph of the drilling equipment; **b** borehole log; **c** gravimetric moisture content.

identified as low-ice permafrost, from 7.6 to 15 m, there is reddish-brown heavily weathered mudstone.

The presence of massive ground ice and high ice content permafrost provides substantial material conditions for the development and evolution of the Gu-hill RTS, indirectly supporting the reason for its large scale. The moisture content curve shown in Fig. 12c further illustrates the ground ice content in this region, indicating that the upper limit of the permafrost is located 2.1 to 2.4 m below the surface. The thickness of the active layer decreases closer to the headwall due to lateral thermal erosion caused by the development and evolution of Gu-hill RTS—a key indicator of active freeze-thaw erosion processes.

Nuclear magnetic resonance

In this study, a Dart sensor utilizing borehole NMR techniques was employed to quantify the total volumetric water content and the hydraulic conductivity of the active layer in the studied RTS area^{61,62}. These measurements are essential for understanding how freeze-thaw cycles alter soil hydraulic properties and contribute to erosion processes. The NMR-Dart logging method, known for its ease of operation and high vertical resolution, is currently widely used for in-situ determination of hydraulic properties. The fundamental principle of borehole NMR logging involves estimating soil permeability by acquiring geometric information about pore spaces and determining the porosity filled with water⁶³. The Dart soil moisture sensing system consists of a Dart control unit, a logging probe, and a field data acquisition computer (Fig. 10b). The logging probe has a diameter of 4.4 cm, a vertical length of 22.9 cm, and a detection range encompassing a 15.2 cm diameter area around the probe center. To enhance the signal-to-noise ratio of the detection results, the Dart sensors record test results at two frequencies: 426.27 kHz and 478.271 kHz⁶⁴. The Schlumberger-Doll Research (SDR) equation was employed to estimate soil hydraulic conductivity (K_{SDR}). This inversion technique, frequently applied in permafrost research, is responsive to thin, low-K strata and is represented as follows:

$$K_{SDR} = C^m T_{2ML}^2 \quad (1)$$

here, C and m denote the lithologic constant and porosity exponent, respectively. Φ represents the fractional porosity, while T_{2ML} refers to the logarithmic mean of the T_2 (decay time) distribution, calculated as:

$$T_{2ML} = \exp\left(\frac{\sum A_i \ln(T_{2i})}{\sum A_i}\right) \quad (2)$$

where A_i correlates with the total number of spins in the i^{th} pore type, which relaxes with a decay time (T_{2i}).

At the three boreholes located on the eastern side of the investigated Gu-hill RTS, a 50 mm diameter PVC probe was inserted, with the bottom sealed to prevent water ingress. A Dart sensor was deployed within the PVC probe to measure soil hydraulic conductivity through a cylindrical shell with a diameter of 15.2 cm, assessing the soil surrounding the probe's center at a vertical resolution of 0.2 m. During each measurement, the Dart probe was maintained at a static depth before being advanced to the next depth. Soil moisture content was measured at 0.5 m intervals. To verify the soil hydraulic conductivity results acquired through Dart sensor, undisturbed soil samples from boreholes were gathered at the study location and examined in the laboratory. Additionally, post-processing analysis of NMR detection data was performed using Vista Clara software. The T_2 decay curve was used to estimate the distribution of soil volumetric water content. Due to soil characteristics, different types of water content were fitted as a function of T_2 decay time. Typically, the T_2 decay time is categorized into three ranges: less than 3.16 ms, 3.16 to 31.6 ms, and greater than 31.6 ms. These ranges correspond to free water, retained water, and bound water, respectively. This detailed characterization of water states is essential for understanding freeze-thaw processes, as laboratory NMR analyses indicated that the unfrozen water content in silt samples ranged from 1% to 10%⁶⁵.

Drawing from prior experience⁴², the unfrozen water in this study was primarily composed of gravitational water ($T_2 > 33$ ms).

Electrical resistivity tomography and ground-penetrating radar

To elucidate the characteristics of ground ice, the permafrost table, and the impacts of freeze-thaw erosion and thermal disturbance on the soil beneath the Gu-hill RTS development area, non-invasive geophysical surveys—specifically, ERT and GPR profiling—were conducted during the thawing season of 2021 and 2022 (Fig. 10). Among the existing near-surface geophysical survey methods, ERT is employed to infer geological or geophysical characteristics based on measurements of subsurface potential differences. It is particularly effective in characterizing permafrost because the resistivity model of permafrost layers is strongly correlated with ground ice content and unfrozen water content—both critical parameters in freeze-thaw erosion processes. Additionally, resistivity is highly sensitive to the transition between the active layer and the underlying permafrost. GPR alongside ERT in the same survey section provides complementary geophysical information. While both GPR and ERT can approximate the position of the permafrost table, GPR is more adept at detecting shallow soil layers such as the active layer and interpreting soil stratification. In contrast, ERT utilizes the resistivity variability of different materials to explore the spatial distribution of various subsurface layers (such as sediments, air, groundwater, and ground ice) and is better suited for investigating permafrost characteristics below the permafrost table, such as ground ice. However, ERT is less effective in determining soil stratification. Therefore, the combined use of ERT and GPR surveys can effectively provide high-resolution interpreted profiles of Gu-hill RTS development areas, inferring the corresponding stratigraphic structures and freeze-thaw induced changes.

In the research area, the spatial distribution of massive ground ice, ice-rich permafrost, and the permafrost table was identified on-site using a testing system based on the Advanced Geosciences Inc. (AGI) Supersting R8. Due to the presence of a substantial amount of mudflow material within the development area of the Gu-hill RTS and the significant height of the headwall, two ERT survey lines were established. One line was positioned 2.5 m south of the headwall (in the east-west direction), and the other 2 m east of the longitudinal (north-south direction) RTS development direction. Each survey line consisted of 48 electrodes spaced 3 meters apart (Fig. 10d, e). Based on previous ERT survey work conducted in the permafrost regions of the QTP^{37,66}, this study employed a dipole-dipole array configuration within the testing system. Current was injected into the ground according to the electrode arrangement, creating a known geometric factor (K), and the apparent resistivity (ρ_s) was measured. The ERT testing system performed extensive measurements by altering different central points and the spacing between two electrodes, resulting in a two-dimensional distribution image of the measured apparent resistivity in both the horizontal (along the survey line direction) and vertical (soil depth direction) planes. The fundamental principles of this process can be described as follows:

$$\rho_s = K \frac{\Delta V}{I} \quad (3)$$

$$K = \frac{2\pi}{\frac{1}{AM} - \frac{1}{AN} - \left(\frac{1}{BM} - \frac{1}{BN}\right)} \quad (4)$$

where ρ_s denotes the apparent resistivity (Ωm); ΔV represents the electrical potential difference (V); I indicates the supplied current (A) and; K is the dimensionless geometric factor. AM , AN , BM , and BN correspond to the distances between pairs of electrodes.

The ERT testing data was inverted for apparent resistivity using the post-processing software EarthImager 2D. Initially, topographic correction was performed based on the field-measured surface elevation and electrode spacing. The software's embedded program employs a regularized least squares method for data inversion, utilizing the Euclidean norm ($L2$ norm) for regularization. The inversion results were selected based on smaller root

mean square errors and L_2 norms closer to 1, ultimately yielding a corresponding two-dimensional resistivity model. This model can represent the true subsurface resistivity distribution. Due to the lack of corresponding resistivity reference values for the strata near the RTS in the QTP development area, the resistivity variations obtained from ERT testing under assumed constant natural conditions (lithology, pore structure, electrodes, etc.) are primarily attributed to changes in unfrozen water content. To better interpret the resistivity values of the permafrost layer in the thermokarst slump area, this study employed a regression equation^{2,28} between unfrozen water content and resistivity, as detailed in the following formula:

$$R = e^{-\frac{\omega_u}{\omega_{u0}}} R_{\omega_{u0}} \quad (5)$$

where R represents the electrical resistivity of permafrost ($\Omega \text{ m}$), $R_{\omega_{u0}}$ denotes the reference electrical resistivity value of $12,820 \Omega \text{ m}$ when the unfrozen water content $\omega_{u0} = 5\%$, and ω_u signifies the unfrozen water content (%).

Given that GPR survey technology has been widely applied to the detection of permafrost, yielding numerous results in the investigation of ground ice, the internal structure of periglacial landforms, and the thickness of the active layer, this paper will not elaborate on the corresponding principles of GPR. In this study, field investigations were conducted using the CrossOver730 (ImpulseRadar) GPR to detect the Gu-hill RTS under investigation, as shown in Fig. 10c. The survey routes were consistent with those of the ERT survey lines. Due to the presence of a substantial amount of mudflow material on the surface of the slump area and the high water content during the thawing season, the GPR results could be adversely affected. Therefore, no surveys were conducted within the development area itself. The selected GPR device integrated antennas with frequencies of 300 MHz and 70 MHz, enabling the acquisition of data at different depths simultaneously. The GPR data were post-processed using ImpulseRadar CrossPoint software, resulting in a two-dimensional dielectric constant profile of the strata after filtering. Ultimately, the iterative interpretation results of the GPR and ERT inversions were comprehensively analyzed and, combined with borehole data, validated the location of the permafrost table and the spatial distribution characteristics of ground ice. Consequently, this study, based on the results of the integrated geophysical surveys, provides geophysical evidence for the permafrost conditions and thermal disturbance characteristics contributing to freeze-thaw erosion in the RTS development area.

Multi-temporal deformation investigation

To quantify soil erosion resulting from freeze-thaw processes in the Gu-hill RTS development area, the TLS-UAV method used in this study was developed in previous studies by the authors⁵. Data acquisition involved high-resolution point clouds and UAV aerial images, captured using the Leica P50 terrestrial laser scanner and the DJI Matrice M300 RTK equipped with Zenmuse P1 and L1 cameras, respectively.

Point cloud processing was carried out using Leica Cyclone 9.2.0 (<https://leica-geosystems.com>), while aero-triangulation and model reconstruction were performed with DJI Terra for the initial post-processing of the collected data. Following basic preprocessing, spatial sampling was conducted to remove extraneous points. Points with a spacing of 0.1 m were then extracted and meshed into time-series triangular irregular networks (TINs). TIN comparisons were subsequently conducted using Matlab 2019b. Detailed analysis procedures are outlined in the authors' previous studies⁵. Through overlay analysis, we quantified the headwall retreat and volumetric changes in the development area of the Gu-hill RTS. This provided a quantitative assessment of soil erosion resulting from freeze-thaw processes in RTS.

Data availability

No datasets were generated or analyzed during the current study.

Received: 14 February 2025; Accepted: 25 March 2025;

Published online: 11 June 2025

References

- Bernhard, P., Zwieback, S., Bergner, N. & Hajnsek, I. Assessing volumetric change distributions and scaling relations of retrogressive thaw slumps across the Arctic. *Cryosphere* **16**, 1–15 (2022).
- Niu, F., Jiao, C., Luo, J., He, J. & He, P. Three-dimensional numerical modeling of ground ice ablation in a retrogressive thaw slump and its hydrological ecosystem response on the Qinghai-Tibet Plateau, China. *Int. J. Disaster Risk Sci.* **14**, 566–585 (2023).
- Sun, Z., Wang, Y., Sun, Y., Niu, F. & Gao, Z. Creep characteristics and process analyses of a thaw slump in the permafrost region of the Qinghai-Tibet Plateau, China. *Geomorphology* **293**, 1–10 (2017).
- Jiang, G. et al. Development of a rapid active layer detachment slide in the Fenghuoshan Mountains, Qinghai–Tibet Plateau. *Permafro. Periglac. Process.* **33**, 298–309 (2022).
- Jiao, C. et al. Deformation and volumetric change in a typical retrogressive thaw slump in permafrost regions of the Central Tibetan Plateau, China. *Remote Sens.* **14**, 5592 (2022).
- Nicu, I. C., Lombardo, L. & Rubensdotter, L. Preliminary assessment of thaw slump hazard to Arctic cultural heritage in Nordenskiöld Land, Svalbard. *Landslides* **18**, 2935–2947 (2021).
- Nesterova, N. et al. Retrogressive thaw slump theory and terminology. *EGUSphere* **2024**, 1–36 (2024).
- Lewkowicz, A. G. & Way, R. G. Extremes of summer climate trigger thousands of thermokarst landslides in a High Arctic environment. *Nat. Commun.* **10**, 1–11 (2019).
- Nicu, I. C., Elia, L., Rubensdotter, L., Tanyaş, H. & Lombardo, L. Multi-hazard susceptibility mapping of cryospheric hazards in a high-Arctic environment: Svalbard Archipelago. *Earth Syst. Sci. Data* **15**, 447–464 (2023).
- Luo, J. et al. Inventory and frequency of retrogressive thaw slumps in permafrost region of the Qinghai–Tibet Plateau. *Geophys. Res. Lett.* **49**, e2022GL099829 (2022).
- Luo, J. et al. Recent rapid initiation and growth of retrogressive thaw slumps in the Hoh Xil region of the Qinghai-Tibetan Plateau. *Catena* **243**, 108158 (2024).
- Peng, X. et al. The first hillslope thermokarst inventory for the permafrost region of the Qilian Mountains. *Earth Syst. Sci. Data* **16**, 2033–2045 (2024).
- Kizyakov, A. I. et al. Landforms and degradation pattern of the Batagay thaw slump, Northeastern Siberia. *Geomorphology* **420**, 108501 (2023).
- Sun, W. et al. Observed permafrost thawing and disappearance near the altitudinal limit of permafrost in the Qilian Mountains. *Adv. Clim. Chang. Res.* **13**, 642–650 (2022).
- Luo, J., Niu, F., Lin, Z., Liu, M. & Yin, G. Recent acceleration of thaw slumping in permafrost terrain of Qinghai-Tibet Plateau: an example from the Beiluhe Region. *Geomorphology* **341**, 79–85 (2019).
- Droppo, I. G., di Cenzo, P., McFadyen, R. & Reid, T. Assessment of the sediment and associated nutrient/contaminant continuum, from permafrost thaw slump scars to tundra lakes in the western Canadian Arctic. *Permafro. Periglac. Process.* **33**, 32–45 (2022).
- Segal, R. A., Lantz, T. C. & Kokelj, S. V. Acceleration of thaw slump activity in glaciated landscapes of the Western Canadian Arctic. *Environ. Res. Lett.* **11**, 034025 (2016).
- Zhou, W. et al. Dramatic carbon loss in a permafrost thaw slump in the Tibetan Plateau is dominated by the loss of microbial necromass carbon. *Environ. Sci. Technol.* **57**, 6910–6921 (2023).
- Mu, M. et al. Topographic drivers of permafrost organic carbon accumulation on the Northern Qinghai–Tibet Plateau. *Permafro. Periglac. Process.* **35**, 373–383 (2024).
- Du, R. et al. Quantitative impact of organic matter and soil moisture on permafrost. *J. Geophys. Res. Atmos.* **128**, e2022JD037686 (2023).
- Xia, Z. et al. Widespread and rapid activities of retrogressive thaw slumps on the Qinghai-Tibet Plateau from 2016 to 2022. *Geophys. Res. Lett.* **51**, e2024GL109616 (2024).

22. Xia, Z. et al. Retrogressive thaw slumps along the Qinghai-Tibet Engineering Corridor: a comprehensive inventory and their distribution characteristics. *Earth Syst. Sci. Data* **14**, 3875–3887 (2022).

23. Wu, T. et al. Spatiotemporal changes of freezing/thawing indices and their response to recent climate change on the Qinghai-Tibet Plateau from 1980 to 2013. *Theor. Appl. Climatol.* **132**, 1187–1199 (2018).

24. Zhao, L. et al. Changing climate and the permafrost environment on the Qinghai-Tibet (Xizang) plateau. *Permafro. Periglac. Process.* **31**, 396–405 (2020).

25. Zhang, G., Nan, Z., Zhao, L., Liang, Y. & Cheng, G. Qinghai-Tibet Plateau wetting reduces permafrost thermal responses to climate warming. *Earth Planet. Sci. Lett.* **562**, 116858 (2021).

26. Ramage, J. L. et al. Terrain controls on the occurrence of coastal retrogressive thaw slumps along the Yukon Coast, Canada. *J. Geophys. Res. Earth Surf.* **122**, 1619–1634 (2017).

27. Niu, F., Luo, J., Lin, Z., Fang, J. & Liu, M. Thaw-induced slope failures and stability analyses in permafrost regions of the Qinghai-Tibet Plateau, China. *Landslides* **13**, 55–65 (2016).

28. Fortier, R., LeBlanc, A. M., Allard, M., Buteau, S. & Calmels, F. Internal structure and conditions of permafrost mounds at Umiujaq in Nunavik, Canada, inferred from field investigation and electrical resistivity tomography. *Can. J. Earth Sci.* **45**, 367–387 (2008).

29. Bussière, L., Schmutz, M., Fortier, R., Lemieux, J. M. & Dupuy, A. Near-surface geophysical imaging of a thermokarst pond in the discontinuous permafrost zone in Nunavik (Québec). *Can. Permafro. Periglac. Process.* **33**, 353–369 (2022).

30. Liu, W., Fortier, R. & Molson, J. A conceptual model for talik dynamics and icing formation in a river floodplain in the continuous permafrost zone at Salluit, Nunavik (Quebec), Canada. *Permafro. Periglac. Process.* **32**, 468–483 (2021).

31. Huang, L., Liu, L., Luo, J., Lin, Z. & Niu, F. Automatically quantifying evolution of retrogressive thaw slumps in Beiluhe (Tibetan Plateau) from multi-temporal CubeSat images. *Int. J. Appl. Earth Obs. Geoinf.* **102**, 102399 (2021).

32. Huang, L., Luo, J., Lin, Z., Niu, F. & Liu, L. Using deep learning to map retrogressive thaw slumps in the Beiluhe region (Tibetan Plateau) from CubeSat images. *Remote Sens. Environ.* **237**, 111534 (2020).

33. Zhang, H., Wang, H., Zhang, J., Luo, J. & Yin, G. Automatic identification of thaw slumps based on neural network methods and thaw slumping susceptibility. *Int. J. Disaster Risk Sci.* **14**, 539–548 (2023).

34. Nicu, I. C., Rubensdotter, L., Tanyaş, H. & Lombardo, L. Near Pan-Svalbard permafrost cryospheric hazards inventory (SvalCryo). *Sci. Data* **11**, 894 (2024).

35. Yang, Y. et al. A collaborative and scalable geospatial data set for Arctic retrogressive thaw slumps with data standards. *Sci. Data* **12**, 18 (2025).

36. He, P. et al. Assessment of diseases in embankment–bridge transition section with methodological detection along the Qinghai-Tibet railway in permafrost regions. *Permafro. Periglac. Process.*, 1–18, <https://doi.org/10.1002/ppp.2267> (2025).

37. Gao, S., Jin, H., Bense, V. F., Wang, X. & Chai, X. Application of electrical resistivity tomography for delineating permafrost hydrogeology in the headwater area of Yellow River on Qinghai-Tibet Plateau, SW China. *Hydrogeol. J.* **27**, 1725–1737 (2019).

38. Liu, W., Fortier, R., Molson, J. & Lemieux, J. Three-dimensional numerical modeling of cryo-hydrogeological processes in a river-talik system in a continuous permafrost environment. *Water Resour. Res.* **58**, e2021WR031630 (2022).

39. Kunz, J. & Kneisel, C. Three-dimensional investigation of an open- and a closed-system Pingo in northwestern Canada. *Permafro. Periglac. Process.* **32**, 541–557 (2021).

40. Moua, R., Lesparre, N. & Girard, J. F. et al. Coupled hydrogeophysical inversion of an artificial infiltration experiment monitored with ground-penetrating radar: synthetic demonstration. *Hydrol. Earth Syst. Sci.* **27**, 4317–4334 (2023).

41. Jiao, C., Wang, Y., Shan, Y., He, P. & He, J. Quantifying the effect of a retrogressive thaw slump on soil freeze-thaw erosion in permafrost regions on the Qinghai-Tibet Plateau, China. *L. Degrad. Dev.* **34**, 2573–2588 (2023).

42. Gao, Z., Niu, F., Wang, Y., Lin, Z. & Wang, W. Suprapermafrost groundwater flow and exchange around a thermokarst lake on the Qinghai-Tibet Plateau, China. *J. Hydrol.* **593**, 125882 (2021).

43. Creighton, A. L. et al. Transient electromagnetic surveys for the determination of talik depth and geometry beneath thermokarst lakes. *J. Geophys. Res. Solid Earth* **123**, 9310–9323 (2018).

44. Zhong, W. et al. Seasonal deformation monitoring over thermokarst landforms using terrestrial laser scanning in Northeastern Qinghai-Tibetan Plateau. *Int. J. Appl. Earth Obs. Geoinf.* **103**, 102501 (2021).

45. Zhou, C., Zhao, P. & Chen, J. The interdecadal change of summer water vapor over the Tibetan Plateau and associated mechanisms. *J. Clim.* **32**, 4103–4119 (2019).

46. Yin, A. & Harrison, T. M. Geologic evolution of the Himalayan-Tibetan orogen. *Annu. Rev. Earth Planet. Sci.* **28**, 211–280 (2000).

47. Royden, L. H., Burchfiel, B. C. & van der Hilst, R. D. The geological evolution of the Tibetan Plateau. *Sci.* **321**, 1054–1058 (2008).

48. Zhang, W., Zhou, T. & Zhang, L. Wetting and greening Tibetan Plateau in early summer in recent decades. *J. Geophys. Res. Atmos.* **122**, 5808–5822 (2017).

49. Chen, H. et al. The impacts of climate change and human activities on biogeochemical cycles on the Qinghai-Tibetan Plateau. *Glob. Chang. Biol.* **19**, 2940–2955 (2013).

50. Zhao, Y., Nan, Z., Ji, H. & Zhao, L. Convective heat transfer of spring meltwater accelerates active layer phase change in Tibetan permafrost areas. *Cryosph. Discuss.* 1–37 <https://doi.org/10.5194/tc-2021-191> (2021).

51. Gao, H. et al. Permafrost hydrology of the Qinghai-Tibet Plateau: a review of processes and modeling. *Front. Earth Sci.* **8**, 576838 (2021).

52. Li, R. et al. Impact of climate warming on permafrost changes in the Qinghai-Tibet Plateau. *Cold Reg. Sci. Technol.* **205**, 103692 (2023).

53. Zhang, Y., et al. Permafrost characteristics and potential influencing factors in the lake regions of Hoh Xil, Qinghai-Tibet Plateau. *Geoderma* **437**, 116572 (2023).

54. Fan, X. et al. Cryostructures and ground ice content in ice-rich permafrost area of the Qinghai-Tibet Plateau with computed tomography scanning. *J. Mt. Sci.* **18**, 1208–1221 (2021).

55. Cheng, G. et al. Characteristic, changes and impacts of permafrost on Qinghai-Tibet Plateau. *Kexue Tongbao/Chin. Sci. Bull.* **64**, 2783–2795 (2019).

56. Cao, B. et al. Permafrost zonation index map and statistics over the Qinghai-Tibet Plateau based on field evidence. *Permafro. Periglac. Process.* **30**, 178–194 (2019).

57. Luo, J. et al. Inventory and frequency of retrogressive thaw slumps in permafrost region of the Qinghai-Tibet Plateau. *Geophys. Res. Lett.* **49**, 1–9 (2022).

58. Lewkowicz, A. G. & Way, R. G. Extremes of summer climate trigger thousands of thermokarst landslides in a High Arctic environment. *Nat. Commun.* **10**, 1329 (2019).

59. Lin, Z., Niu, F., Liu, H. & Lu, J. Hydrothermal processes of Alpine Tundra Lakes, Beiluhe Basin, Qinghai-Tibet Plateau. *Cold Reg. Sci. Technol.* **65**, 446–455 (2011).

60. Lou, P. et al. Recognition of thaw slumps based on machine learning and UAVs: A case study in the Qilian Mountains, northeastern Qinghai-Tibet Plateau. *Int. J. Appl. Earth Obs. Geoinf.* **116**, 103163 (2023).

61. Niu, F., Gao, Z., Lin, Z., Luo, J. & Fan, X. Vegetation influence on the soil hydrological regime in permafrost regions of the Qinghai-Tibet Plateau, China. *Geoderma* **354**, (2019).

62. Gao, Z., Lin, Z., Niu, F. & Luo, J. Soil water dynamics in the active layers under different land-cover types in the permafrost regions of the Qinghai–Tibet Plateau, China. *Geoderma* **364**, 114176 (2020).
63. Dlubac, K. et al. Use of NMR logging to obtain estimates of hydraulic conductivity in the High Plains aquifer, Nebraska, USA. *Water Resour. Res.* **49**, 1871–1886 (2013).
64. Walsh, D. et al. A small-diameter nmr logging tool for groundwater investigations. *Groundwater* **51**, 914–926 (2013).
65. Yoshikawa, K. & Overduin, P. P. Comparing unfrozen water content measurements of frozen soil using recently developed commercial sensors. *Cold Reg. Sci. Technol.* **42**, 250–256 (2005).
66. You, Y., Yu, Q., Pan, X., Wang, X. & Guo, L. Application of electrical resistivity tomography in investigating depth of permafrost base and permafrost structure in Tibetan Plateau. *Cold Reg. Sci. Technol.* **87**, 19–26 (2013).

Acknowledgements

This study was fully supported by the Strategic Priority Research Program of the Chinese Academy of Sciences (XDB0950000), the National Natural Science Foundation of Guangdong Province (2025A1515011344), the Science Fund for Distinguished Young Scholars of Gansu Province (24JRRRA077), the Tertiary Education Scientific research project of Guangzhou Municipal Education Bureau (2024312551), and the Youth Innovation Talent Project, Guangdong Provincial Department of Education (2024KQNCX210).

Author contributions

C.J. conducted the geophysical data survey and interpretation, wrote the manuscript, and created the figures. P.H. provided data analysis support. F.Y. contributed field survey data. F.N. and J.L. provided critical feedback and comments on the manuscript. All authors participated in the revision and finalization of the manuscript.

Competing interests

The authors declare no competing interests.

Additional information

Correspondence and requests for materials should be addressed to Fujun Niu.

Reprints and permissions information is available at <http://www.nature.com/reprints>

Publisher's note Springer Nature remains neutral with regard to jurisdictional claims in published maps and institutional affiliations.

Open Access This article is licensed under a Creative Commons Attribution-NonCommercial-NoDerivatives 4.0 International License, which permits any non-commercial use, sharing, distribution and reproduction in any medium or format, as long as you give appropriate credit to the original author(s) and the source, provide a link to the Creative Commons licence, and indicate if you modified the licensed material. You do not have permission under this licence to share adapted material derived from this article or parts of it. The images or other third party material in this article are included in the article's Creative Commons licence, unless indicated otherwise in a credit line to the material. If material is not included in the article's Creative Commons licence and your intended use is not permitted by statutory regulation or exceeds the permitted use, you will need to obtain permission directly from the copyright holder. To view a copy of this licence, visit <http://creativecommons.org/licenses/by-nc-nd/4.0/>.

© The Author(s) 2025